Emergence of topological and trivial interface states in VSe_2 films coupled to Bi_2Se_3

Joseph A. Hlevyack,[1,*] Yang-Hao Chan,[2,3,*] Meng-Kai Lin,[1,4,*] Tao He,[2] Wei-Hsiang Peng,[1] Ellen C. Royal,[1] Mei-Yin Chou,[2,5,†] and T.-C. Chiang[1,‡]

[1]*Department of Physics and Frederick Seitz Materials Research Laboratory, University of Illinois at Urbana-Champaign, Urbana, Illinois 61801, USA*

[2]*Institute of Atomic and Molecular Sciences, Academia Sinica, Taipei 10617, Taiwan*

[3]*Physics Division, National Center for Theoretical Sciences, Taipei 10617, Taiwan*

[4]*Department of Physics, National Central University, Taoyuan 32001, Taiwan*

[5]*Department of Physics, National Taiwan University, Taipei 10617, Taiwan*

(Received 2 December 2021; revised 8 April 2022; accepted 27 April 2022; published 12 May 2022)

Coupling ordinary metals with topological Bi_2Se_3 can instigate the long-range migration of the spin-polarized Dirac states. Instead, for trivial metallic VSe_2 films on Bi_2Se_3, topological and trivial Rashba-type interface states emerge, each strongly localized at the VSe_2/Bi_2Se_3 interface. Their rapidly decaying spectral weights are uncovered by thickness-dependent band mappings of VSe_2 films and replicated by a phenomenological first-principles model of the spectral function. The results are pertinent to spintronic devices requiring spin transmission across metal/topological insulator interfaces.

DOI: 10.1103/PhysRevB.105.195119

I. INTRODUCTION

Fundamental to future impetus regarding topological insulators (TIs) is integration of TIs into heterostructures exhibiting emergent phenomena [1–4], whereby Dirac states are judiciously tuned while fostering a myriad of exotic quasiparticle excitations ranging from Majorana fermions to magnetic skyrmions [1–14]. By virtue of symmetry-protected emergent quasiparticles, hybrid topological systems hold alluring promises for applications in fault-tolerant quantum computation, spintronics, and low-power electronics [4]. Though mandated in topological devices containing TIs, ordinary metal contacts interfaced with TIs such as Bi_2Se_3 happen to be intriguing, albeit the simplest, cases for probing hybridization coupling between trivial and nontrivial phases [7–11]. Theoretically, when trivial metals contact TIs, topological surface states couple with bulk metallic states, thereby potentially spawning topological quantum well resonances having nontrivial spin textures that propagate over extended distances [7]. Indeed, as recently demonstrated by angle-resolved photoemission spectroscopy (ARPES), band mappings of superconducting Pb overlayers on $TlBiSe_2$ exhibit the migration of nontrivial states, as exact clones of those on pure $TlBiSe_2$, to the probed Pb surface over appreciable distances (up to ∼5 nm) [8]. Still, nontrivial surface bands can instead be converted into topological interface states (TISs) localized at the trivial material/TI interface [10–14]. Nevertheless, confirming the presence and band tuning of TISs in topological heterostructures has been impeded—or even overlooked—due to often-low photoemission spectral weights of interface states [10], inhomogeneity of overlaying films [9–11], and/or inherent difficulties of first-principles modeling of real hybrid systems with exceedingly large unit cells under full atomic relaxations [8,15].

Herein, we unveil complete evidence from thickness-dependent ARPES for concomitant evolutions of two species of spin-polarized surface states, one nontrivial and the other trivial Rashba-type [16–18], into interfacial bands in thin-film heterostructures of topological Bi_2Se_3 and trivial metallic VSe_2, all corroborated by a fresh first-principles model for the spectral function. Topologically trivial VSe_2 itself possesses an exotic charge density wave in the single-layer limit distinct from that in bulk [19–21], which also evidently suppresses the theoretically predicted ferromagnetic phase for pristine single-layer VSe_2 [19–23]. When fabricated on topological Bi_2Se_3, VSe_2 emerges as a cardinal system harboring strongly localized nontrivial and trivial Rashba-type states. As the VSe_2 thickness varies from zero to three layers, all surface bands of Bi_2Se_3 transfigure into interfacial states with substantially reduced spectral weights and the Dirac cone preserved, vanishing in the mappings at three layers due to photoemission's superficial probing depth [24,25]. First-principles modeling of the spectral functions and wave functions' charge densities reinforces the inception of these interface states. Our results provide methodologies for probing localized symmetry-protected states in real hybrid systems and underscore engineering constraints of topological devices.

II. METHODS

Before thin-film growths with molecular beam epitaxy (MBE), 6*H*-SiC(0001) substrates were annealed repeatedly to ∼1300 °C, yielding bilayer-graphene-terminated SiC

*These authors contributed equally to this work.
†mychou6@gate.sinica.edu.tw
‡tcchiang@illinois.edu

(BLG/SiC). To fabricate Bi_2Se_3 films, Bi and Se were coevaporated from an electron-beam evaporator and an effusion cell, respectively, onto BLG/SiC held at 220 °C; the growth rate was one quintuple layer (QL) (1 QL ≈ 1 nm) every ∼12.5 min, and Bi_2Se_3 films were postannealed for ∼45 min at 220 °C under Se flux [26,27]. VSe_2 films were prepared by codepositing V and Se onto 10 QL Bi_2Se_3 and BLG/SiC at 280 °C; the growth rate was ∼50 min per triatomic layer (TL) (1 TL ≈ 0.6 nm). Deposition rates were cross-checked *in situ* with a quartz crystal monitor and ARPES through established methods [15,19,26–30]. Photoemission measurements were undertaken at 30 K with 21.218-eV photons using a Scienta R4000 analyzer and a Scienta-Omicron VUV5k He lamp. Sharp reflection high-energy electron diffraction (RHEED) patterns for all $N = 0$–3 TL VSe_2 films on 10 QL Bi_2Se_3 and BLG/SiC also confirmed *in situ* the samples' high crystallinity [30].

First-principles calculations were executed using a localized basis set under the linear combination of atomic orbitals method implemented in SIESTA [31–34]. The generalized gradient approximation with the Perdew-Burke-Ernzerhof functional [35] was employed to calculate atomic-layer-resolved, orbital-projected band structures. Though VSe_2 and Bi_2Se_3 lattices are incommensurate with in-plane lattice constants $a_V = 3.357$ Å for VSe_2 and $a_B = 4.143$ Å for Bi_2Se_3 differing by ∼19% [36,37], their structural parameters grant a near lattice matching for a superlattice with periodicity $5a_V \cong 4a_B$. Consequently, computations of VSe_2/Bi_2Se_3 entailed superlattices having an in-plane periodicity $5a_V = 4a_B$ at zero twist angle (with $a_V = 3.314$ Å), each modeled as periodic slab systems with vacuum gaps larger than 14.1 Å. A k-space mesh of 4×4 was used; spin-orbit interactions and the dipole correction were incorporated. Unfolded band structures were computed using the utility in SIESTA [38], modified to handle energy bands with spin-orbit coupling included. The lattice structure of atomic layers in the first Bi_2Se_3 QL and VSe_2 TL nearest to the VSe_2/Bi_2Se_3 interface was optimized separately via VASP [39,40] using the Perdew-Burke-Ernzerhof functional with the van der Waals D2 correction [41], until the residual force on each atom was less than 10^{-3} eV/Å and with the total energy difference less than 10^{-6} eV.

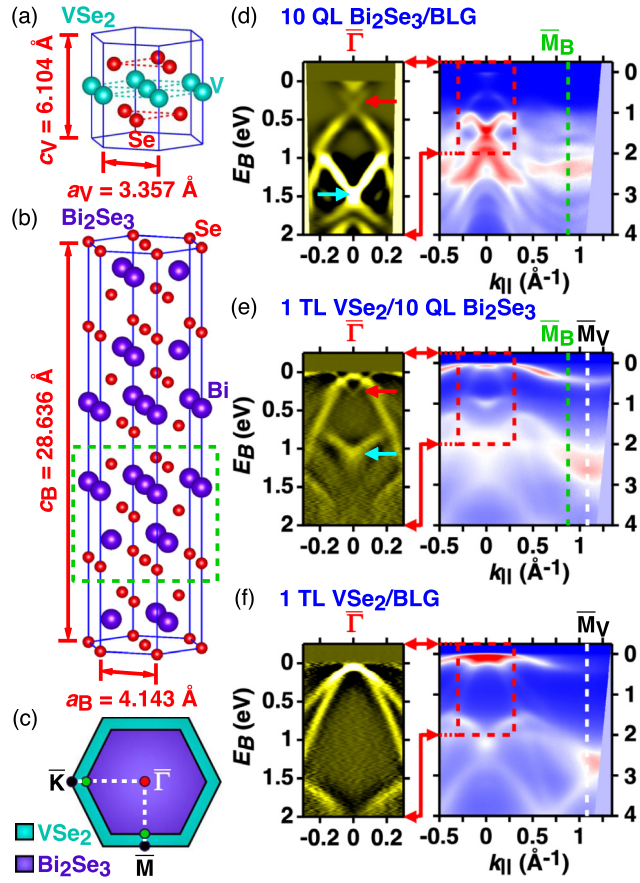

FIG. 1. Contrasting components in VSe_2/Bi_2Se_3. (a) Unit cell for VSe_2 TL. (b) Atomic structure of Bi_2Se_3 (QL identified with green dashed rectangle). (c) Comparisons between surface Brillouin zones of VSe_2 (turquoise) and Bi_2Se_3 (violet); $\overline{\Gamma M}$ lengths are 1.081 Å^{-1} for VSe_2 and 0.875 Å^{-1} for Bi_2Se_3. (d) Second-derivative spectra near the Fermi level (left) and wide-range band mapping (right) for 10 QL Bi_2Se_3/BLG, taken at 30 K with 21.218-eV photons. The topological Dirac cone (red arrow) and trivial Rashba spin-split surface states (cyan arrow) are marked. (e) Same as (d) but for 1 TL VSe_2/10 QL Bi_2Se_3; Dirac-cone-like (red arrow) and V-shaped (cyan arrow) features are distinguished. (f) Same as (e) but for 1 TL VSe_2/BLG. In (d)–(f), second derivatives are taken along the in-plane momentum direction; $\bar{M}$ points of Bi_2Se_3 and VSe_2 are designated.

III. RESULTS AND DISCUSSION

One VSe_2 TL typically adopts the 1T lattice structure [Fig. 1(a)], wherein three triangular atomic layers of V and Se are stacked in the order Se-V-Se [19–23], while Bi_2Se_3 manifests a rhombohedral phase [Fig. 1(b)] consisting of QL units, each terminated by Se layers and assembled as a stack of alternating triangular atomic layers of Bi and Se [16]. Bulk VSe_2 (Bi_2Se_3) is constructed by vertically stacking, while preserving inversion symmetry, many TLs (QLs) with adjacent TLs (QLs) weakly held together by van der Waals bonds. The crystallographic orientation of VSe_2 TLs on Bi_2Se_3 surfaces aligns with that of Bi_2Se_3 [Figs. 1(c)–1(f)] [16–21,30]. For comparisons, Fig. 1(c) schematically depicts the (001)-projected Brillouin zone of Bi_2Se_3 overlaid on that for VSe_2. Second-derivative band mapping of 10 QL Bi_2Se_3/BLG near the Fermi level [Fig. 1(d), left panel] uncovers sharp topological surface states and intense quasiparticle signals from trivial Rashba spin-split surface bands [17,18], hallmarks of smooth TI surfaces [18,26–29]. Probing the band structure of 10 QL Bi_2Se_3/BLG over extended measurement ranges [Fig. 1(d)] unveils numerous crisp valence bands [18,29]. After deposition of 1 TL VSe_2 onto 10 QL Bi_2Se_3, a weakly dispersive feature near the Fermi level dominates ARPES and second-derivative mappings, while other zone-centered, holelike bands disperse strongly down into valence bands buried at deeper binding energies [Fig. 1(e)]. Such bands are quintessential to VSe_2 [Fig. 1(f)], with the former and latter primarily derived from V 3d and Se 4p orbitals, respectively [9,19–21]. No ferromagnetic exchange splitting emerges [Figs. 1(d)–1(f)], suggesting pristine VSe_2 films here are nonferromagnetic [9,19–21]. However, for 1 TL

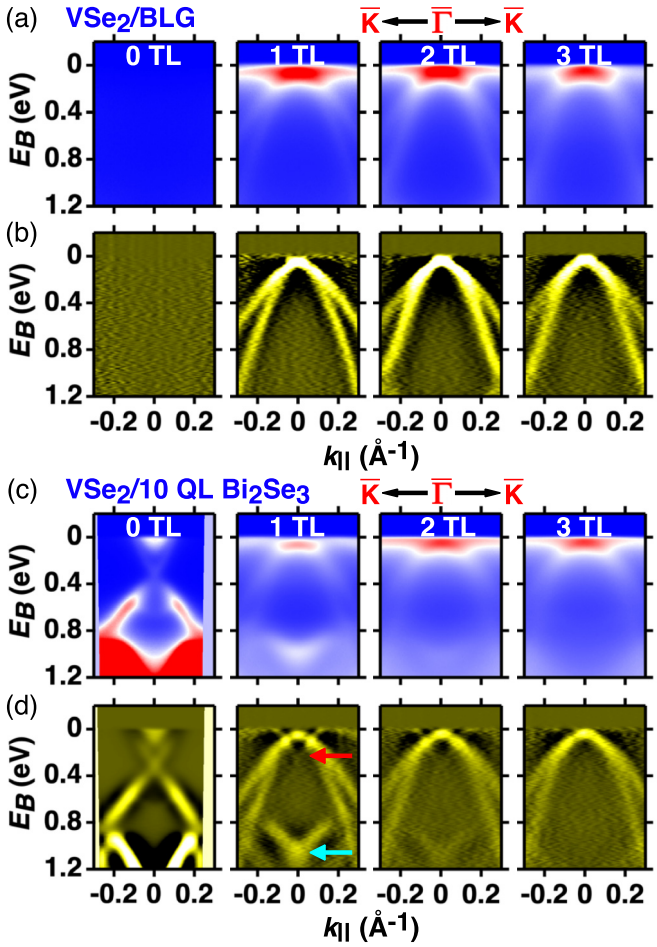

FIG. 2. Topological and trivial interface states in VSe_2/Bi_2Se_3. (a), (b) ARPES maps near the Fermi level along $\overline{\Gamma K}$ and corresponding second derivatives with respect to the in-plane momentum for $N = 0$–3 TL VSe_2/BLG, respectively, taken at 30 K using 21.218-eV photons. (c), (d) Same as (a), (b) but for $N = 0$–3 TL VSe_2/10 QL Bi_2Se_3; interfacial bands TISs (red arrow) and SISs (cyan arrow) are marked in (d).

VSe_2/10 QL Bi_2Se_3, besides a V-shaped structure centered at the $\bar{\Gamma}$ point, a clear Dirac-cone-like feature arises in the second derivative near the Fermi level [Fig. 1(e), left panel], largely obscured in the raw data by the more intense V 3*d* and Se 4*p* bands [Fig. 2]. Undoubtedly, these two band features arise from interfacing VSe_2 with Bi_2Se_3, per their absence in 1 TL VSe_2/BLG results [Fig. 1(f)].

Since two species of surface states abound on Bi_2Se_3 [Fig. 1(d)] [17,18], one hypothesis for the Dirac-cone-like and V-shaped structures of 1 TL VSe_2/10 QL Bi_2Se_3 is they are interface states derived, respectively, from topological and trivial Rashba spin-split surface bands of Bi_2Se_3, corroborated by their reduced spectral weights and slight energy shifts relative to those of pristine Bi_2Se_3 [Figs. 1(d) and 1(e)] [10–12]. Such presumed TISs and their "sister" interface states (SISs)—TISs for the Dirac-cone-like feature and SISs for the V-shaped structure—should exhibit greatly attenuated spectral weights with further increase of the VSe_2 thickness due to photoemission's short probing depth, about 1 nm [24,25], comparable to the thickness of 2 TL VSe_2 [per Fig. 1(a)]. Figures 2(a) and 2(b) summarize ARPES and second-derivative spectra near the Fermi level along $\overline{\Gamma K}$ for $N = 0$–3 TL VSe_2/BLG; similar datasets for $N = 0$–3 TL VSe_2/10 QL Bi_2Se_3 appear in Figs. 2(c) and 2(d). Aside from evident V-shaped SISs in the spectra for 1 TL and 2 TL VSe_2/10 QL Bi_2Se_3, both sets of ARPES maps for $N = 1$–3 TL VSe_2 are superficially similar to one another [Figs. 2(a) and 2(c)]. Second derivatives highlight contrasts: For 1 TL VSe_2/10 QL Bi_2Se_3, the Dirac cone of the TISs and the SISs emerge [Fig. 2(d)], both absent in 1 TL VSe_2/BLG data [Fig. 2(b)]; further increase of film thickness to 2 TL in VSe_2/10 QL Bi_2Se_3 yields dramatic reductions in spectral weights of the TISs and SISs, which disappear at 3 TL [Fig. 2(d)]. Conversely, besides the trivial instance when the thickness is tuned from 0 to 1 TL, second-derivative spectra for VSe_2/BLG here vary little with thickness [Fig. 2(b)].

To rationalize these thickness-mediated evolutions and unambiguously recognize the TISs and SISs as interfacial entities, spectral functions $P(k_{||}, E_B)_N$ for $N = 0$–2 TL VSe_2/6 QL Bi_2Se_3 are calculated by summing over theoretical atomic-layer-resolved band structures $L(i, k_{||}, E_B)_N$ [30], each modulated by an effective cross section factor $R_i = \sigma_i/\sigma_{Bi}$ for the *i*th layer's atomic species (Se 4*p*, V 3*d*, or Bi 6*p*) and an exponentially decaying weight in the position z_i along the *c* axis (referenced to the probed surface) introduced by photoemission [24,25]:

$$\frac{P(k_{||}, E_B)_N}{\sigma_{Bi}} = \sum_i R_i \exp(-z_i/\lambda) L(i, k_{||}, E_B)_N. \quad (1)$$

The photoelectrons' escape depth is set to $\lambda = 8.75$ Å, consistent for an incident photon energy of 21.218 eV [24], while $R_{Se} = 0.05$ and $R_V = 0.075$ ($R_{Bi} = 1$) through experimentation [30]. These results were Gaussian broadened using full width at half maxima of 125 meV and 0.06 $Å^{-1}$ for binding energy and momentum broadenings, respectively, and then multiplied by the Fermi-Dirac distribution at 30 K. Figures 3(a) and 3(b) present measured mappings along $\overline{\Gamma K}$ for $N = 0$–2 TL VSe_2/10 QL Bi_2Se_3 and their second derivatives, while simulated spectra along $\overline{\Gamma K}$ and associated second derivatives for $N = 0$–2 TL VSe_2/6 QL Bi_2Se_3 appear in Figs. 3(c) and 3(d). For completeness, similar experimental and theoretical datasets along $\overline{\Gamma M}$ appear in the Supplemental Material [30]. Like the ARPES and second-derivative maps for 10 QL Bi_2Se_3 [Figs. 3(a) and 3(b)], simulations for 6 QL Bi_2Se_3 exhibit ungapped topological surface states [Figs. 3(c) and 3(d)] [26,28]. Upon addition of 1 TL VSe_2, these surface states are replaced by a Dirac-cone-like feature in the simulated derivative [Fig. 3(d)], like the observed TISs [Fig. 3(b)]. As in the ARPES map [Fig. 3(a)], these simulated TISs are largely masked by VSe_2 bands in the calculated mapping [Fig. 3(c)]. Likewise, V-shaped SISs unmistakably arise in the simulated 1 TL data [Figs. 3(c) and 3(d)]. Although the binding energy position of the calculation's SIS feature deviates from that observed [Figs. 3(b) and 3(d)], such discrepancies are expected considering similar differences between experimental and first-principles results reported for trivial Rashba-type surface states of Bi_2Se_3 and oft-unavoidable Se vacancies in MBE-grown compounds, which foster shifts in surface/interfacial and bulk bands [18,26–29]. Increasing the

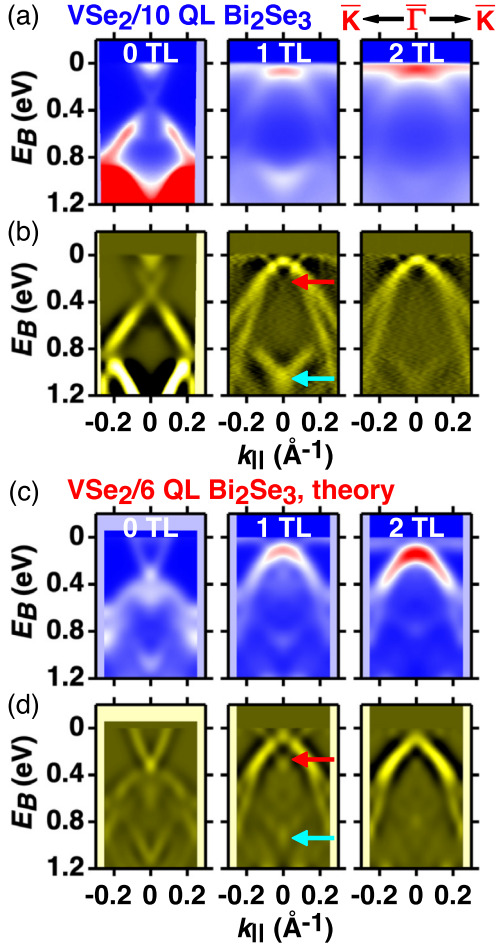

FIG. 3. Thickness-dependent ARPES versus simulated maps. (a), (b) Photoemission mappings and corresponding second derivatives for $N = 0$–2 TL $VSe_2/10$ QL Bi_2Se_3, respectively, measured along $\overline{\Gamma K}$ at 30 K with 21.218-eV photons. (c), (d) Theoretical spectral functions and their second derivatives for $N = 0$–2 TL $VSe_2/6$ QL Bi_2Se_3, respectively, calculated parallel to $\overline{\Gamma K}$. In (b), (d), second derivatives are along the in-plane momentum direction; TISs (red arrow) and SISs (cyan arrow) are flagged.

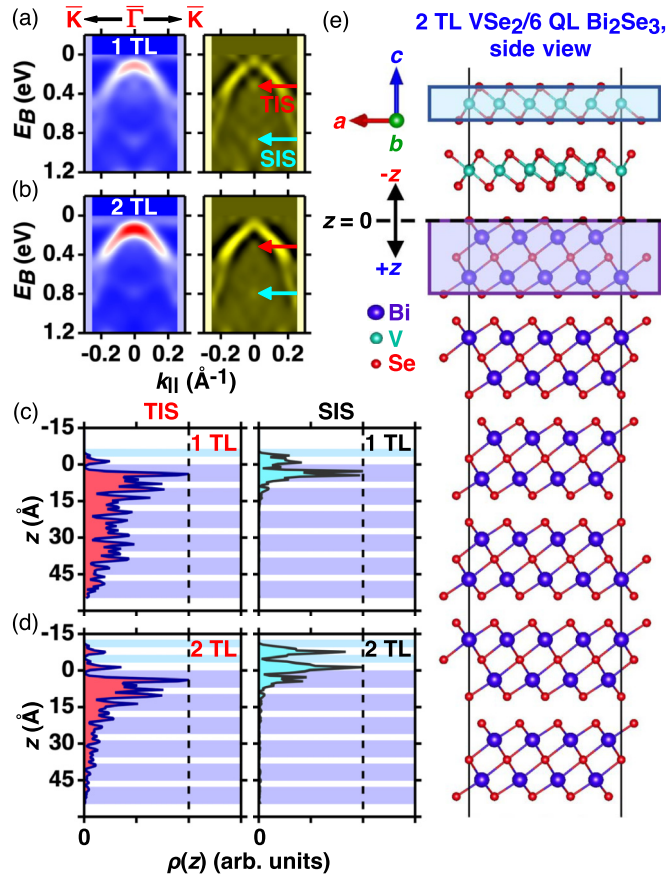

FIG. 4. Spatial charge densities for interface states. (a) Simulated mapping (left) along $\overline{\Gamma K}$ and its second derivative with respect to the in-plane momentum (right) for 1 TL $VSe_2/6$ QL Bi_2Se_3, wherein TISs (red arrow) and SISs (cyan arrow) are identified. (b) Similar to (a) but for 2 TL $VSe_2/6$ QL Bi_2Se_3. (c) Integrated charge densities ρ for TISs (left) and SISs (right) of 1 TL $VSe_2/6$ QL Bi_2Se_3 at the $\overline{\Gamma}$ point graphed versus the spatial coordinate z along the c axis, where $z = 0$ is at the top Se layer of Bi_2Se_3. Each curve is normalized to its maximum; colored rectangles mark regions occupied by atomic layers of Bi_2Se_3 (lavender) and VSe_2 (turquoise). (d) Same as (c) but for 2 TL $VSe_2/6$ QL Bi_2Se_3. (e) Side view of 2 TL $VSe_2/6$ QL Bi_2Se_3 lattice overlaid with turquoise and lavender rectangles for select VSe_2 and Bi_2Se_3 atomic-layer sets, respectively, acting as guides to those in (c), (d).

VSe_2 thickness to 2 TL suppresses the spectral weights for the simulated TISs and SISs, though hints remain [Figs. 3(c) and 3(d)]. Overall, the simulations' dimensionality-mediated behaviors remarkably complement our experimental evidence for the localized natures of the TISs and SISs.

Furthermore, the interfacial characters of the TISs and SISs, ones with wave functions spatially concentrated around the VSe_2/Bi_2Se_3 interface, are extracted from the states' thickness-dependent charge densities. Figures 4(a) and 4(b) reproduce simulated mappings and their second derivatives for 1 TL and 2 TL $VSe_2/6$ QL Bi_2Se_3. At both VSe_2 thicknesses, spatial charge densities ρ for TISs and SISs at the $\overline{\Gamma}$ point, integrated in real space over the in-plane coordinates, are plotted in Figs. 4(c) and 4(d) versus the coordinate z along the c direction, as defined in the lattice in Fig. 4(e). For TISs [Figs. 4(c) and 4(d), left panels], the charge density mostly lies within the first couple of Bi_2Se_3 QLs nearest the VSe_2/Bi_2Se_3 interface, though there are non-negligible penetrations of the wave functions into the van der Waals gap(s) of overlaying VSe_2. As for SISs [Figs. 4(c) and 4(d), right panels], the largest contribution is concentrated near the VSe_2/Bi_2Se_3 interface, but the wave functions penetrate significantly into VSe_2 over an extended z range, implying the SISs are more accessible with photoemission than the TISs [Figs. 4(c) and 4(d)], consistent with the measurements [Figs. 3(a) and 3(b)].

IV. CONCLUSION

Transformations of topological and trivial Rashba spin-split surface bands into interfacial phenomena in VSe_2/Bi_2Se_3 are extreme antitheses of potential long-range migrations of topological states into trivial metals [7,8]. Signatures of interfacial states in VSe_2/Bi_2Se_3, namely,

dramatic reductions in spectral weights with increasing VSe_2 thickness [Figs. 2(c) and 2(d)], are understood in terms of photoemission's probing depth—here, ∼1 nm [24,25]—which limits observing bands spatially localized near the VSe_2/Bi_2Se_3 interface, per our simulations [Figs. 3 and 4]. Such localized behaviors are relevant when refining designs for nanoscale devices requiring transmissions of spin polarization across metallic/TI interfaces [7]. Moreover, these conversions leave tantalizing features, including topological Dirac states, largely intact, though interfacial band dispersions are visibly modified relative to those of Bi_2Se_3 despite weak incommensurate van der Waals bonding at the interface [Fig. 3]. These preservations amid hybridization coupling are critical prerequisites for exploiting TIs in topological devices [4–8]. Thus, our work not only helps complete the picture for hybridization coupling effects in trivial metal/TI but also highlights methods for probing localized topological and trivial Rashba-type states, while revealing design limitations of topologically protected states in spintronic devices.

ACKNOWLEDGMENTS

This work was supported by the U.S. Department of Energy (DOE), Office of Science (OS), Office of Basic Energy Sciences, Division of Materials Science and Engineering, under Grant No. DE-FG02-07ER46383 (T.-C.C.). Y.-H.C., T.H., and M.-Y.C. acknowledge support from Academia Sinica, Taiwan. Y.-H.C. acknowledges support by the Ministry of Science and Technology (Grant No. 110-2124-M-002-012), National Center for Theoretical Sciences, and National Center for High-Performance Computing in Taiwan. M.-K.L acknowledges support from the Ministry of Science and Technology of Taiwan under Grant No. MOST 110-2112-M-008-039-MY3.

[1] L. Fu and C. L. Kane, Superconducting Proximity Effect and Majorana Fermions at the Surface of a Topological Insulator, Phys. Rev. Lett. **100**, 096407 (2008).

[2] K. Yasuda, R. Wakatsuki, T. Morimoto, R. Yoshimi, A. Tsukazaki, K. S. Takahashi, M. Ezawa, M. Kawasaki, N. Nagaosa, and Y. Tokura, Geometric Hall effects in topological insulator heterostructures, Nat. Phys. **12**, 555 (2016).

[3] J. Chen, L. Wang, M. Zhang, L. Zhou, R. Zhang, L. Jin, X. Wang, H. Qin, Y. Qiu, J. Mei, F. Ye, B. Xi, H. He, B. Li, and G. Wang, Evidence for magnetic skyrmions at the interface of ferromagnet/topological-insulator heterostructures, Nano Lett. **19**, 6144 (2019).

[4] X.-L. Qi and S.-C. Zhang, Topological insulators and superconductors, Rev. Mod. Phys. **83**, 1057 (2011).

[5] B.-J. Yang, M. S. Bahramy, and N. Nagaosa, Topological protection of bound states against the hybridization, Nat. Commun. **4**, 1524 (2013).

[6] T. Shoman, A. Takayama, T. Sato, S. Souma, T. Takahashi, T. Oguchi, K. Segawa, and Y. Ando, Topological proximity effect in a topological insulator hybrid, Nat. Commun. **6**, 6547 (2015).

[7] X. Wang, G. Bian, T. Miller, and T.-C. Chiang, Topological quantum well resonances in metal overlayers, Phys. Rev. B **87**, 235113 (2013).

[8] C. X. Trang, N. Shimamura, K. Nakayama, S. Souma, K. Sugawara, I. Watanabe, K. Yamauchi, T. Oguchi, K. Segawa, T. Takahashi, Y. Ando, and T. Sato, Conversion of a conventional superconductor into a topological superconductor by topological proximity effect, Nat. Commun. **11**, 159 (2020).

[9] T. Yilmaz, X. Tong, Z. Dai, J. T. Sadowski, E. F. Schwier, K. Shimada, S. Hwang, K. Kisslinger, K. Kaznatcheev, E. Vescovo, and B. Sinkovic, Emergent flat band electronic structure in a VSe_2/Bi_2Se_3 heterostructure, Commun. Mater. **2**, 11 (2021).

[10] Y. A. Surnin, I. I. Klimovskikh, D. M. Sostina, K. A. Kokh, O. E. Tereshchenko, and A. M. Shikin, Impact of ultrathin Pb films on the topological surface and quantum-well states of Bi_2Se_3 and Sb_2Te_3 topological insulators, J. Exp. Theor. Phys. **126**, 535 (2018).

[11] A. Eich, N. Rollfing, F. Arnold, C. Sanders, P. R. Ewen, M. Bianchi, M. Dendzik, M. Michiardi, J.-L. Mi, M. Bremholm, D. Wegner, P. Hofmann, and A. A. Khajetoorians, Absence of superconductivity in ultrathin layers of FeSe synthesized on a topological insulator, Phys. Rev. B **94**, 125437 (2016).

[12] C. M. Polley, R. Buczko, A. Forsman, P. Dziawa, A. Szczerbakow, R. Rechciński, B. J. Kowalski, T. Story, M. Trzyna, M. Bianchi, A. G. Čabo, P. Hofmann, O. Tjernberg, and T. Balasubramanian, Fragility of the Dirac cone splitting in topological crystalline insulator heterostructures, ACS Nano **12**, 617 (2018).

[13] R. Yoshimi, A. Tsukazaki, K. Kikutake, J. G. Checkelsky, K. S. Takahashi, M. Kawasaki, and Y. Tokura, Dirac electron states formed at the heterointerface between a topological insulator and a conventional semiconductor, Nat. Mater. **13**, 253 (2014).

[14] M. H. Berntsen, O. Götberg, B. M. Wojek, and O. Tjernberg, Direct observation of decoupled Dirac states at the interface between topological and normal insulators, Phys. Rev. B **88**, 195132 (2013).

[15] M.-K. Lin, T. He, J. A. Hlevyack, P. Chen, S.-K. Mo, M.-Y. Chou, and T.-C. Chiang, Coherent electronic band structure of $TiTe_2/TiSe_2$ moiré bilayer, ACS Nano **15**, 3359 (2021).

[16] H. Zhang, C.-X. Liu, X.-L. Qi, X. Dai, Z. Fang, and S.-C. Zhang, Topological insulators in Bi_2Se_3, Bi_2Te_3 and Sb_2Te_3 with a single Dirac cone on the surface, Nat. Phys. **5**, 438 (2009).

[17] H.-H. Kung, A. P. Goyal, D. L. Maslov, X. Wang, A. Lee, A. F. Kemper, S.-W. Cheong, and G. Blumberg, Observation of chiral surface excitons in a topological insulator Bi_2Se_3, Proc. Natl. Acad. Sci. USA **116**, 4006 (2019).

[18] Y. Xia, D. Qian, D. Hsieh, L. Wray, A. Pal, H. Lin, A. Bansil, D. Grauer, Y. S. Hor, R. J. Cava, and M. Z. Hasan, Observation of a large-gap topological-insulator class with a single Dirac cone on the surface, Nat. Phys. **5**, 398 (2009).

[19] P. Chen, W. W. Pai, Y.-H. Chan, V. Madhavan, M. Y. Chou, S.-K. Mo, A.-V. Fedorov, and T.-C. Chiang, Unique Gap Structure and Symmetry of the Charge Density Wave in Single-Layer VSe_2, Phys. Rev. Lett. **121**, 196402 (2018).

[20] J. Feng, D. Biswas, A. Rajan, M. D. Watson, F. Mazzola, O. J. Clark, K. Underwood, I. Marković, M. McLaren, A. Hunter, D. M. Burn, L. B. Duffy, S. Barua, G. Balakrishnan, F. Bertran, P. Le Fèvre, T. K. Kim, G. van der Laan, T. Hesjedal, P. Wahl *et al.*, Electronic structure and enhanced charge-density wave order of monolayer VSe_2, Nano Lett. **18**, 4493 (2018).

[21] P. M. Coelho, K. N. Cong, M. Bonilla, S. Kolekar, M.-H. Phan, J. Avila, M. C. Asensio, I. I. Oleynik, and M. Batzill, Charge density wave state suppresses ferromagnetic ordering in VSe_2 monolayers, J. Phys. Chem. C **123**, 14089 (2019).

[22] Y. Ma, Y. Dai, M. Guo, C. Niu, Y. Zhu, and B. Huang, Evidence of the existence of magnetism in pristine VX_2 monolayers (X = S, Se) and their strain-induced tunable magnetic properties, ACS Nano **6**, 1695 (2012).

[23] M. Bonilla, S. Kolekar, Y. Ma, H. C. Diaz, V. Kalappattil, R. Das, T. Eggers, H. R. Gutierrez, M.-H. Phan, and M. Batzill, Strong room-temperature ferromagnetism in VSe_2 monolayers on van der Waals substrates, Nat. Nanotechnol. **13**, 289 (2018).

[24] M. P. Seah and W. A. Dench, Quantitative electron spectroscopy of surfaces: A standard data base for electron inelastic mean free paths in solids, Surf. Interface Anal. **1**, 2 (1979).

[25] S. Hüfner, *Photoelectron Spectroscopy*, 3rd ed. (Springer-Verlag, New York, 2003).

[26] D. Flötotto, Y. Ota, Y. Bai, C. Zhang, K. Okazaki, A. Tsuzuki, T. Hashimoto, J. N. Eckstein, S. Shin, and T.-C. Chiang, Superconducting pairing of topological surface states in bismuth selenide films on niobium, Sci. Adv. **4**, eaar7214 (2018).

[27] J. A. Hlevyack, S. Najafzadeh, M.-K. Lin, T. Hashimoto, T. Nagashima, A. Tsuzuki, A. Fukushima, C. Bareille, Y. Bai, P. Chen, R.-Y. Liu, Y. Li, D. Flötotto, J. Avila, J. N. Eckstein, S. Shin, K. Okazaki, and T.-C. Chiang, Massive Suppression of Proximity Pairing in Topological $(Bi_{1-x}Sb_x)_2Te_3$ Films on Niobium, Phys. Rev. Lett. **124**, 236402 (2020).

[28] Y. Zhang, K. He, C.-Z. Chang, C.-L. Song, L.-L. Wang, X. Chen, J.-F. Jia, Z. Fang, X. Dai, W.-Y. Shan, S.-Q. Shen, Q. Niu, X.-L. Qi, S.-C. Zhang, X.-C. Ma, and Q.-K. Xue, Crossover of the three-dimensional topological insulator Bi_2Se_3 to the two-dimensional limit, Nat. Phys. **6**, 584 (2010).

[29] T. J. Whitcher, M. G. Silly, M. Yang, P. K. Das, D. Peyrot, X. Chi, M. Eddrief, J. Moon, S. Oh, A. H. Castro-Neto, M. B. H. Breese, A. T. S. Wee, F. Silly, and A. Rusydi, Correlated plasmons in the topological insulator Bi_2Se_3 induced by long-range electron correlations, NPG Asia Mater. **12**, 37 (2020).

[30] See Supplemental Material at http://link.aps.org/supplemental/10.1103/PhysRevB.105.195119 for additional experimental data and theoretical analysis, including Refs. [7–9,15–21,24–29].

[31] P. Ordejón, E. Artacho, and J. M. Soler, Self-consistent order-*N* density-functional calculations for very large systems, Phys. Rev. B **53**, R10441 (1996).

[32] D. Sánchez-Portal, P. Ordejón, E. Artacho, and J. M. Soler, Density-functional method for very large systems with LCAO basis sets, Int. J. Quantum Chem. **65**, 453 (1997).

[33] J. M. Soler, E. Artacho, J. D. Gale, A. García, J. Junquera, P. Ordejón, and D. Sánchez-Portal, The SIESTA method for *ab initio* order-*N* materials simulation, J. Phys.: Condens. Matter **14**, 2745 (2002).

[34] E. Artacho, E. Anglada, O. Diéguez, J. D. Gale, A. García, J. Junquera, R. M. Martin, P. Ordejón, J. M. Pruneda, D. Sánchez-Portal, and J. M. Soler, The SIESTA method; developments and applicability, J. Phys.: Condens. Matter **20**, 064208 (2008).

[35] J. P. Perdew, K. Burke, and M. Ernzerhof, Generalized Gradient Approximation Made Simple, Phys. Rev. Lett. **77**, 3865 (1996).

[36] S. Barua, M. C. Hatnean, M. R. Lees, and G. Balakrishnan, Signatures of the Kondo effect in VSe_2, Sci. Rep. **7**, 10964 (2017).

[37] S. Nakajima, The crystal structure of $Bi_2Te_{3-x}Se_x$, J. Phys. Chem. Solids **24**, 479 (1963).

[38] S. G. Mayo, F. Yndurain, and J. M. Soler, Band unfolding made simple, J. Phys.: Condens. Matter **32**, 205902 (2020).

[39] G. Kresse and J. Furthmüller, Efficient iterative schemes for *ab initio* total-energy calculations using a plane-wave basis set, Phys. Rev. B **54**, 11169 (1996).

[40] G. Kresse and D. Joubert, From ultrasoft pseudopotentials to the projector augmented-wave method, Phys. Rev. B **59**, 1758 (1999).

[41] S. Grimme, Semiempirical GGA-type density functional constructed with a long-range dispersion correction, J. Comput. Chem. **27**, 1787 (2006).